AIAA 99-3559

X-33 Computational Aeroheating Predictions and Comparisons with Experimental Data

Brian R. Hollis, Thomas J. Horvath, Scott A. Berry, H. Harris Hamilton II, and Stephen J. Alter

NASA Langley Research Center, Hampton, VA 23681

33rd AIAA Thermophysics Conference

June 28 - July 1, 1999 / Norfolk, VA

X-33 Computational Aeroheating Predictions and Comparisons with Experimental Data

Brian R. Hollis*, Thomas J. Horvath†, Scott A. Berry†,
H. Harris Hamilton II‡, and Stephen J. Alter§
NASA Langley Research Center, Hampton, VA 23681

The goal of the NASA Reusable Launch Vehicle (RLV) technology program is to develop and demonstrate essential, cost-effective technologies for next-generation launch systems. The X–33 flight vehicle presently being developed by Lockheed-Martin is an experimental Single-Stage-to-Orbit (SSTO) demonstrator that is intended to validate critical technologies for the full-scale RLV. One of the key technologies to be demonstrated on the X–33 vehicle is an advanced, metallic thermal protection system (TPS). As part of the development of this TPS system, the aeroheating environment of the X-33 is being defined through conceptual analysis, ground-based wind-tunnel testing and computational fluid dynamics (CFD). This report provides an overview of the hypersonic aeroheating CFD research conducted at the NASA Langley Research Center (LaRC) in support of this TPS development activity. In this research, laminar and turbulent aeroheating predictions were generated at wind-tunnel test conditions for the X–33 vehicle using both a finite-volume, Navier-Stokes solver, and a coupled inviscid-solver/boundary-layer-code engineering method. Computations were performed for angles-of-attack of 20˚, 30˚, and 40˚. Comparisons between the predictions and wind tunnel data for the centerline and axial heating distributions were generally within ±10% for the Navier-Stokes method and ±25% for the engineering code method. Aeroheating distributions were also computed for the peak heating point on the flight trajectory.

Nomenclature

H	enthalpy (J/kg)
h	heat transfer coefficient (kg/m^2-sec), $h = \dot{q}/(H_{aw} - H_w)$
h_{FR}	Fay-Riddell heating coefficient (kg/m^2-sec)
L	reference length (m)
M	Mach number
p	pressure (N/m^2)
$\dot{q}$	heat transfer rate (W/m^2)
Re	Reynolds number
T	temperature (K)
U_∞	freestream velocity (m/sec)
X, Y, Z	coordinate system (m)
α	angle-of-attack (deg)
ρ	density (kg/m^3)

Introduction

The Access to Space Study[1] conducted by NASA recommended the development of a fully Reusable Launch Vehicle (RLV)[2,3,4] to provide a next-generation launch capability at greatly reduced cost. This recommendation led to the RLV/X–33 technology program, an industry-led effort in partnership with NASA. As part of this program, the X–33 is intended to serve as a sub-scale technology demonstrator for a full-scale Single-Stage-to-Orbit (SSTO) RLV. The X–33 is intended to prove the feasibility of the SSTO-RLV concept through demonstration of key design and operational aspects of the vehicle.

Following a Phase I industry competition between several aerospace companies, the Lockheed-Martin lifting-body concept was selected by NASA for award of the Phase II contract to design, develop and construct an X–33 flight vehicle. The Lockheed-Martin X–33 design[5], shown in Fig. 1, is a half-scale version of an RLV, and incorporates a delta-shape lifting-body planform, symmetric canted fins, twin vertical tails and dual body flaps for aerodynamic control, and a linear aerospike engine for propulsion.

As part of the X–33 industry/government partnership, the NASA Langley Research Center (LaRC) was tasked to provide aerodynamic performance data, surface aeroheating distributions, and boundary-layer transition correlations to Lockheed-Martin to support Phase II aerodynamic and aerothermodynamic

* Aerospace Technologist, Aerothermodynamics Branch, Aero-and-Gas Dynamics Division, Member AIAA
† Aerospace Technologist, Aerothermodynamics Branch, Aero-and-Gas Dynamics Division
‡ Aerospace Technologist, Aerothermodynamics Branch, Aero-and-Gas Dynamics Division, Associate Fellow AIAA
§ Aerospace Technologist, Senior Member AIAA

design and development. In order to provide these data, a synergistic experimental/computational research program was conducted at NASA LaRC.

Early results from the LaRC X–33 research program were presented in Refs. 6 and 7. In those works, data from early Phase II aeroheating wind tunnel tests were presented and compared with laminar and turbulent predictions generated using both a Navier-Stokes solver and a boundary-layer engineering code[7]. These early results were used to formulate and support the use of an Re_θ/M_e criteria for predicting transition onset on the X–33 in flight[6].

Since the above-mentioned research was published, additional wind tunnel tests and computations have been performed to supplement the original data base with more detailed results and to accommodate design changes to the original X–33 configuration. Key results of recent Phase II experimental and computational aeroheating research are presented in this reference and in two companion papers by Horvath et al[8] and Berry et al[9]. Experimental and computational aerodynamic research will be presented in two forthcoming papers by Murphy et al[10] and Hollis et al[11].

In the present paper, laminar and turbulent Navier-Stokes and boundary-layer engineering code predictions for the aeroheating environment of the X–33 at hypersonic wind tunnel test conditions are presented and compared with experimental data from Refs. 8 and 9. Computational issues including grid resolution and adaption, turbulence modeling, and inviscid flux formulations are also discussed. Finally, computations are presented for the peak heating on a sample X–33 flight trajectory.

X-33 Geometry

The computational results presented in this reference are based on the 604B0002F configuration of the Lockheed-Martin X–33 vehicle, which is commonly referred to as the F–Loft, Rev–F configuration. A brief history of the X–33 configuration evolution through Phase II of the program is presented in Ref. 8. The current F–Loft, Rev–F configuration (Fig. 1) is a lifting-body delta planform with twin vertical tails, canted fins and body flaps. The body length is 19.3 m (63.2 ft.) from the nose to the end of the engine module, and the span across the canted fins is 8.11 m (36.6 ft). The canted fins have a dihedral of 20-deg and a -8.58-deg incidence angle. While some changes in the X–33 configuration have occurred since this research began, they were not of enough significance to warrant updating the computational modeling of the geometry.

Computational Methods

Numerical Algorithms

Computational predictions for comparison with the wind tunnel aeroheating test data were generated using two methods: a Navier-Stokes solver, GASP[12], and an engineering method in which the LATCH[13] boundary layer code and an inviscid solution from the LAURA[14,15] code were employed to compute surface heating distributions. Both GASP and LATCH/LAURA computations were performed with a laminar, perfect-gas thermochemical model at freestream conditions of Mach 6 with a Reynolds number of 4.0×10^6/ft. Turbulent computations were also performed at the same Reynolds number using the GASP code. Finally, laminar, reacting gas computations for the peak heating point along a sample trajectory were performed using both GASP and LAURA.

The GASP (General Aerodynamic Simulation Program) code[12] is a three-dimensional, finite-volume Navier-Stokes solver which incorporates numerous flux formulations, thermochemical models, turbulence models, and time-integration methods. A perfect-gas air model was used for the wind tunnel test cases discussed in this paper, and an equilibrium air model was used for the trajectory case. The Jacobi scheme was used for time-integration. Full viscous terms were retained for all three directions and modeled with second-order central differences. As will be detailed in the "Flux Splitting and Grid Resolution" section, a third-order, upwind biased, min-mod limited scheme, which consisted of a Roe[16] flux formulation in the body-normal direction and a Van Leer[17] formulation in the other two directions, was employed to represent the inviscid fluxes. The turbulent computations were performed using the algebraic Baldwin-Lomax model with Gupta's[18] pressure gradient and compressibility corrections with the entire flow field treated as turbulent.

The LATCH (Langley Approximate Three-Dimensional Convective Heating) code[13] is a three-dimensional boundary layer code based on the axisymmetric analog[19] for general three-dimensional boundary layers. An approximate integral heating method[20] is used to compute the heating rates along three-dimensional inviscid streamlines. The inviscid streamlines must be supplied from separate, three-dimension inviscid flow field computations, which were generated with the LAURA code in this work.

The LAURA (Langley Aerothermodynamic Upwind Relaxation Algorithm) code[14, 15] is a three-dimensional Navier-Stokes solver based on a point-

relaxation scheme and Roe[16] averaging with Yee's[21] Symmetric Total Variation Diminishing limiter for inviscid fluxes. The code includes perfect-gas, equilibrium and non-equilibrium air models. For the present work, inviscid solutions were generated for use with LATCH using a perfect-gas air model. A trajectory computation was also performed using a non-equilibrium air model.

Boundary Conditions

The Mach 6, $Re_\infty = 4.0x10^6$/ft freestream flow conditions for the GASP and LATCH/LAURA computations were taken from those of aeroheating tests[8,9] conducted in the NASA LaRC 20-Inch Mach 6 Air Tunnel, which is described in Ref. 22. Nominal conditions for this case are listed in Table 1. The wall boundary condition for the computations was fixed at a uniform ambient (300 K) temperature. This approximation is valid, because an aeroheating run in this tunnel is of short enough duration such that the increase in model surface temperature can be neglected.

Table 1. Freestream Conditions for Wind Tunnel Case Computations

$M_\infty = 5.99$	$Re_{\infty,L} = 3.33x10^6$
$T_\infty = 62.1$ K	$h_{FR} = 0.539$ kg/m^2-sec
$\rho_\infty = 0.0628$ kg/m^3	$\alpha = 20°$, 30°, and 40°

Grid Generation and Adaption

The GASP flow field computations were performed on a (127 x 181 x 65)-point, single-block, half-body grid[23] (Fig. 2). The grid scale was 1.32% that of the full-size X-33 vehicle. This scale was chosen to be identical to that of the wind tunnel models tested in Refs. 8 and 9, which corresponds to a length of 0.254 m (10.0-in.) from the nose of the vehicle to the end of the engine module. The engine-module and wake were not included in this grid, and a fake-wake, solid-body representation was employed for the regions between the canted fins and the end of the body flaps and between the body flaps. The exclusion of the wake from the grid is expected to have a negligible effect on the computations, except perhaps at the end of the fuselage, as only local surface quantities (i.e. convective heating and pressure) are of interest, as opposed to integrated aerodynamic quantities such as the pitching moment.

For each angle-of-attack case, grid adaption was performed to align the outer domain of the grid with the bow shock and to cluster grid points within the wall boundary layer. Typically, the outer boundary was adjusted so that the shock was located at approximately 80% of the normal distance between the wall and outer grid boundary. Approximately 50% of the normal grid points were clustered within the wall boundary layer, and the wall cell Reynolds number was set in the range of 10 to 20. The scheme employed to perform these manipulations is based on Reference 15. When necessary, additional grid quality refinement and smoothing was performed using the Volume Grid Manipulation code[24].

Flux Splitting and Grid Resolution

As mentioned previously, the GASP code incorporates a number of different flux functions including the Roe[16], Van Leer[17], and Roe-Harten[25] schemes. Several test cases were computed to determine the suitability of these schemes for viscous hypersonic flow field computations. The test cases were: Van Leer flux in all three computational directions (referred to as VLVLVL), Roe flux in the normal direction with Van Leer in the other two directions (VLVLRo), Roe-Harten flux in the normal direction with Van Leer in the other two directions (VLVLRH), Roe flux in all directions (RoRoRo), and Roe-Harten flux in the normal direction with the Roe scheme in the other two directions (RoRoRH). For all test cases, a third-order flux formulation with a min-mod Total Variation Diminishing (TVD) limiter was employed. The freestream conditions for these test cases were those of the Mach 6, $Re_\infty = 4.0x10^6$/ft wind tunnel case with $\alpha = 40°$. Centerline heating predictions generated with each of these methods are shown in Fig. 3.

As shown in Fig. 3, the choice of flux functions has a large influence on surface heating computations. The use of Roe's flux in the normal direction is known to produce numerical instabilities around the stagnation region, which can be seen in the discontinuous heating distribution near the nose for the RoRoRo case. Harten's correction in the RoRoRH method dampens out the numerical instability, but introduces excessive dissipation which elevates the heating rates. (It should be noted that the Roe-Harten implementation in GASP is not the same as that in LAURA; in LAURA, the Harten entropy correction has been further modified to produce less dissipation, as documented in Ref. 15) The three cases run with Van Leer's flux (VLVLVL, VLVLRH, and VLVLRo) all produced smooth solutions with varying amounts of numerical dissipation depending on the normal-direction flux. Of the options employed, the case with the Roe flux in the normal direction and Van Leer in the other directions (VLVLRo) produced the smoothest distribution with the least dissipation (i.e. produced the lowest heating rates) and is thus assumed to be the best

solution method of the options available in GASP. The validity of this assumption will be demonstrated in the next section where heating predictions generated using the VLVLRo method are compared with experimental data

After establishing that the VLVLRo method produced the best results, the influence of the TVD limiters on the solution was investigated. Additional cases were run using the VLVLRo scheme with the Superbee[26] and Chakravarthy-Osher[27] limiters in place of the min-mod limiter in the body-normal direction. As shown in Fig. 4, the magnitude of the centerline heating distributions showed much less sensitivity to the limiter than was observed for the flux formulations. However, both the Superbee and Chakravarthy-Osher limited solutions showed a lack of smoothness along the body. It was therefore concluded that the VLVLRo scheme with min-mod limiting produced the best results.

All GASP computational results presented in the rest of this paper were generated with the VLVLRo scheme and the min-mod limiter on a (127 x 181 x 65)-point grid. This grid-point density was determined to be sufficient through a grid resolution study which is shown in Figs. 5-8. In these figures, surface heating distributions computed on this grid as well as on grids with one-half and one-quarter the point density of the original grid are shown along the centerline of the vehicle and at three axial stations. As can be seen in these figures, the computed heating distributions decreased by approximately 10-20% between the coarse grid and the intermediate grid, but dropped by only 5-8% between the intermediate and fine grids. These results suggest that the error due to grid resolution for results obtained on the fine grid is no more than 2-3%. Furthermore, the fairly good accuracy of the results obtained on the intermediate grid using GASP's third-order inviscid flux representation suggests that preliminary design computations for a vehicle such as the X–33 could be performed rapidly on a coarser grid, and that only the final design computations need be performed on a fine grid.

Experiment Background

The experimental aeroheating tests which complement this computational study are presented in detail in Refs. 8 and 9. The goal of these tests was to define the overall aeroheating environment of the X–33 vehicle and to examine the effects of discrete and distributed roughness on boundary layer transition. To date, the aeroheating test program includes over 1100 runs in three different hypersonic wind tunnels. The experimental data referenced in the present work were acquired in the NASA LaRC 20-Inch Mach 6 Air Tunnel. Size and performance information for this facility can be found in Micol[22].

Aeroheating tests in this tunnel were conducted across a range of Reynolds numbers from 1.0×10^6/ft to 7.0×10^6/ft at angles-of-attack from 0° to 40° with body flap deflections of 0°, 10°, and 20° Aeroheating data were obtained in these tests using the two-color, relative intensity, phosphor thermography technique[28]. The aeroheating data were then reduced and analyzed using the IHEAT code[28]. The global data produced by this technique permit the resolution of complex flow phenomena such as transition fronts, vortex structures and shock interactions. Comparisons of phosphor thermography results with computations have been presented in Refs. 7 and 29.

As discussed in Ref. 28, the accuracy of the phosphor technique is dependent on the temperature rise on the surface of the test model. For the windward side heating measurements, the accuracy of the phosphor system is estimated to be approximately ±8%, and the overall experimental uncertainty of the heating data due to all factors is estimated to be ±15%. Because the leeside temperature increase is only a few degrees during a test, the experimental uncertainty for leeside heating rates increases to at least ±25%.

Computations and Comparisons with Experimental Data

Results from GASP and LATCH/LAURA computations will be presented in this section, and comparisons will be made with experimental data. The heating distributions will be presented in terms of the ratio h/h_{FR}. The quantity h_{FR} is a reference heat-transfer coefficient, where: the wall heating rate, $\dot{q}$, is based on Fay-Riddell[30] theory for a hemisphere of the same radius as the nose of X-33 model (1.60 cm); the adiabatic wall enthalpy, $H_{aw,}$ is assumed to be equal to the total tunnel enthalpy, $H_{T,2}$; and the wall enthalpy is computed at an ambient (300 K) wall temperature. Geometric positions are given in non-dimensional form, X/L, Y/L, Z/L, where L is the reference length (10.0-in.) of the wind tunnel model. All computational results for the wind tunnel comparisons were generated at the Mach 6, $Re_\infty = 4.0 \times 10^6$/ft conditions given in Table 1.

Global Heating Comparisons

Graphical comparisons of predicted and measured windward heating distributions for angles-of-attack of 20°, 30°, and 40° are presented in Figs. 9-14. In these figures, wind tunnel heating data, in the form

of two-dimensional images obtained with the thermographic phosphor system, have been mapped onto the three-dimensional surface of the CFD grid. This new option in the IHEAT[28] code permits direct comparisons of heating rates at all points on the body for which heating data have been obtained.

Windward surface views of the comparisons between GASP heating predictions and wind tunnel data for angles-of-attack of 20°, 30°, and 40° are shown in Figs. 9-11, while front views for each case are shown in Figs. 12-14. In these figures, gray indicates regions where no experimental data were obtained because that area of the vehicle was out of the field of view of the camera. In general, agreement between measured and predicted heating rates appears good, although the GASP solutions exhibit higher heating along the chines, while the experimental data exhibit more sharply-defined heating patterns for the shock-interactions on the canted fins.

Laminar Centerline and Axial Cut Comparisons

For a detailed quantitative assessment of the agreement between experimental data and computations, heating distributions were extracted from both sets of data along the centerline of the vehicle and at various axial stations along the body. These quantitative comparisons between predicted and measured windward and leeward heating distributions are presented in Figs 15-26. Laminar GASP and LATCH windward and leeward centerline distributions for angles-of-attack of 20°, 30°, and 40° are compared with experimental data in Figs 15-20. Laminar GASP and LATCH distributions for axial stations of X/L = 0.05, 0.10, 0.20, 0.32, 0.45 and 0.90 for the α=30° case are compared with experimental data in Figs. 21-26. In each of these figures, experimental heating distributions extracted from the global heating images using the IHEAT code for Reynolds numbers of 1.0×10^6/ft to 7.0×10^6/ft are provided for comparison with the 4.0×10^6/ft Reynolds number predictions. Note that in these experimental data, natural transition from laminar flow was observed in the wind tunnel tests[8,9] near the end of the X–33 fuselage on the windward surface at freestream Reynolds number of 4.0×10^6/ft and higher. Therefore, significant differences between the laminar predictions and the experimental data can be expected toward the end of the fuselage for test data where $Re_\infty \geq 4.0 \times 10^6$/ft.

As shown in Figs. 15-17, the laminar GASP predictions for the X–33 windward centerline are within ±10% or less of the laminar ($Re_\infty < 4.0 \times 10^6$/ft) data along the full length of the vehicle for all angles-of-attack except in the low-heating region near the end of the fuselage at α = 20°. Note that the estimated experimental uncertainty on the windward side is approximately ±15%. The LATCH boundary layer results are in close agreement with the experimental data only along the first third of the vehicle; beyond that point the LATCH results are substantially higher than wind tunnel data.

As shown in Figs. 18-20, the laminar GASP predictions for the X–33 leeward centerline are generally within the experimental uncertainty (±25% for the leeside) for all angles-of-attack except for the middle of the fuselage at α = 20° and near the end of the fuselage for α = 30° and 40°. The discrepancies at the end of the fuselage may be due to the fact the expansion of the flow into the wake of the vehicle is not included in the GASP computation due to the use of the fake-wake grid. This expansion does occur in the wind tunnel tests, and might be the cause of the heating increase at the end of the vehicle seen in the experimental data.

In the windward-surface axial cut comparisons of Figs. 21-26, close agreement between the laminar GASP predictions and experimental data is again observed at each of the axial stations. In the areas along the chines near the nose of the vehicle, the differences between the GASP computations and the data are slightly larger than on the rest of the windward surface ~15%), but are still within the estimated uncertainty. It should also be noted that away from the centerline, the LATCH computations are in much better agreement with both GASP results and the wind tunnel data and fall within the experimental uncertainty. This result would suggest that centerline comparisons alone may not provide sufficient information for a complete code validation study.

Turbulent Centerline Comparisons

For the present work, the algebraic Baldwin-Lomax model in the GASP code was modified to include the pressure gradient and compressibility corrections detailed by Gupta[18]. These corrections have been shown to produce significant reductions in computed heating rates which result in good comparisons with experimental heating data[18,31]. As shown in Fig. 27, the X–33 windward centerline heating distributions computed with the modified Baldwin-Lomax method were up to 30-40% lower than those computed with the original method. In Figs. 28-30, these computations are compared with experimental data in which transitional or turbulent boundary layers were produced both naturally and by an array of 0.005-in. height trips placed near the nose of the vehicle[9]. The un-tripped data cover a wide range of Reynolds numbers over which the state of the boundary layer appears to vary from fully laminar to transitional at the

end of the fuselage, so direct comparison with the fully turbulent computations is not appropriate; however qualitative agreement is observed at the higher Reynolds numbers. In the tripped data set, the trips appear to produce fully-developed turbulent flow over most of the vehicle, and the turbulent GASP heating predictions compare with these data to within the estimated experimental uncertainty (±15%) for all three angles-of-attack.

Flight Predictions

With the above experimental comparisons serving to validate the methodolgy (grid resolution, flux functions, limiters, turbulence model) used for GASP heating predictions, several aeroheating computations were performed for flight conditions using GASP. Results for a sample case, the peak heating point (which is laminar) for an early design trajectory referred to as Michael 9A-8 are shown here. Freestream conditions for this case are given in Table 2.

Table 2. Freestream Conditions for Michael 9A-8 Trajectory Peak Heating Point

$M_\infty = 8.83$	$Re_{\infty,L} = 2.07 \times 10^6$
$T_\infty = 265.9$ K	$\alpha = 10.0^\circ$
$\rho_\infty = 7.04 \times 10^{-4}$ kg/m^3	

Given the relatively low Mach number for this case, an equilibrium air chemistry model was employed with a radiative wall temperature boundary condition. The wall emissivity was fixed at 0.85. As a result of the grid resolution study presented earlier, it was also decided that a lower density grid (64 x 91 x 65) could be employed for these computations. Note that as flap deflections for flight were not yet known at the time of work, the flaps were omitted from the computations.

In Figs. 31-38, the GASP predictions for this case are compared to an existing LAURA solution. In the LAURA computations, a high-density (217 x 181 x 65 points) grid was employed along with a non-equilibrium air chemistry model. A fully-catalytic wall boundary condition was specified for the LAURA computation.

Global heating distribution comparisons for the windward and leeward surfaces are presented in Figs. 31 and 32. Detailed centerline and axial heating distributions at two stations are presented for the windward and leeward sides of the vehicle in Figs. 33-38. The global comparisons suggest good agreement between the GASP and LAURA computations. The line cut comparisons show the two solution agree to within less than ±10% except on parts of the centerline toward the end of the fuselage (Figs. 33-34) and on the leeward side of the canted fins (Fig. 38). As very close agreement was obtained on the nose, where non-equilibrium effects would be greatest, the differences on the fins and toward the end of the body are likely due to the lower grid density used in the streamwise and tangential directions for the GASP computations.

Summary and Conclusions

As part of the X–33 Thermal Protection System development program, computational aeroheating solutions for the X–33 Phase II vehicle were generated using both a Navier-Stokes code and an engineering code to complement wind tunnel testing at NASA LaRC. The computations were performed at wind tunnel test conditions of Mach 6 with a 4.0×10^6/ft Reynolds number for angles-of-attack of 20°, 30°, and 40°. Laminar computations were performed using the LATCH boundary layer code with inviscid solutions from the LAURA code, and both laminar and turbulent solutions were generated with the GASP code. Heating distributions at the peak heating point along a sample trajectory were also computed with both GASP and LAURA.

Comparisons were made along the X-33 windward and leeward centerline and at several windward axial locations between the computations and experimental aeroheating data from tests at Reynolds numbers of 1.0×10^6/ft to 7.0×10^6/ft. The estimated uncertainty of these data was ±15% on the windward surface and ±25% on the leeward surface. Windward laminar GASP centerline predictions were generally within ±10% of the laminar experimental data, while leeward predictions were generally within ±25%. Away from the centerline, the GASP windward axial comparisons were also within ±10% of the experimental data except around the chines at the nose of the vehicle, where the agreement was within ±15%. LATCH/LAURA predictions were within ±15% of the data for the first third of the vehicle but were significantly higher than the data along the remainder of the vehicle. However, away from the centerline, the LATCH/LAURA windward axial comparisons were in close agreement with the experimental data. Turbulent windward centerline predictions from GASP with a modified Baldwin-Lomax model were 30-40% lower than heating rates predicted with the un-modified scheme and agreed with turbulent wind tunnel data to within ±15%. Predicted GASP and LAURA distributions for the peak flight heating point were found to agree to within less than ±10% except on the leeside canted fins and parts of the centerline.

Acknowledgements

The authors wish to offer thanks to several NASA LaRC researchers who assisted in this work: Chris Riley generated the LAURA inviscid flow field solutions used in the LATCH computations presented in the paper; Ron Merski provided support and development work for the IHEAT software used in the reduction and analysis of wind tunnel phosphor data and three-dimensional mapping of the data; Rick Thompson generated the LAURA flight case solution; and Chris Glass provided advice in the use of the GASP code.

References

1. Bekey, I., Powell, R., and Austin, R., "NASA Studies Access to Space," Aerospace America, May 1994, pp. 38-43.

2. Cook, S. A., "X–33 Reusable Launch Vehicle Structural Technologies," AIAA Paper 97-10873, Nov. 1996.

3. Freeman Jr., D. C., Talay, T. A, and Austin, R. E., "Reusable Launch Vehicle Technology Program," AIAA Paper IAF 96-V.4.01, Oct., 1996.

4. Powell, R. W., Lockwood, M. K, and Cook, S. A., "The Road from the NASA Access-to-Space Study to a Reusable Launch Vehicle," AIAA Paper IAF-98-V.4.02, Sept. 1998.

5. Baumgartner, R. I., and Elvin, J. D., "Lifting Body - An Innovative RLV Concept," AIAA Paper 95-3531, Sept. 1995.

6. Thompson, R. A., Hamilton II, H. H., Berry, S. A., and Horvath, T. J., "Hypersonic Boundary Layer Transition for X–33 Phase II Vehicle," AIAA Paper 98-0867, Jan., 1998.

7. Hamilton II, H. H., Weilmuenster, K. J., Berry, S. A., and Horvath, T. J., "Computational/ Experimental Aeroheating Predictions for X–33 Phase II Vehicle," AIAA Paper 98-0869, Jan. 1998.

8. Horvath, T. J, Berry, S. A., Hollis, B. R., Liechty, D. S., Hamilton II, H. H., Merski, N. R., "X–33 Experimental Aeroheating at Mach 6 Using Phosphor Thermography," AIAA Paper 99-3558, June 1999.

9. Berry, S. A., Horvath, T. J., Hollis, B. R., Thompson, R. A., Hamilton II, H. H., "X–33 Hypersonic Boundary Layer Transition," AIAA Paper 99-3560, June 1999.

10. Murphy, K. J., Nowak, R. J., Hollis, B. R., and Thompson, R. A., "X–33 Hypersonic Aerodynamic Characteristics," AIAA 99-4162, Aug. 1999.

11. Hollis, B. R., Thompson, R. A., Murphy, K. J, and Nowak, R. J, "X–33 Aerodynamic/ Aerothermodynamic CFD Validation and Flight Predictions," AIAA Paper 99-4163, Aug. 1999.

12. AeroSoft, "GASP Version 3, The General Aerodynamic Simulation Program, Computational Flow Analysis Software for the Scientist and Engineer, User's Manual," AeroSoft Inc., Blacksburg, VA, May 1996.

13. Hamilton, II, H. H., Greene, F. A., and DeJarnette, F. R., "Approximate Method for Calculating Heating Rates on Three-Dimensional Vehicles," *Journal of Spacecraft and Rockets*, Vol. 31, No. 3, May-June 1994, pp. 345-354.

14. Gnoffo, P. A., "An Upwind-Biased, Point-Implicit Algorithm for Viscous, Compressible Perfect-Gas Flows," NASA TP 2953, Feb. 1990.

15. Cheatwood, F. M., and Gnoffo, P. A., "User's Manual for the Langley Aerothermodynamic Upwind Relaxation Algorithm (LAURA)," NASA TM 4674, April, 1996.

16. Roe, P. L., "Approximate Riemann Solvers, Parameter Vectors and Difference Schemes," J*ournal of Computational Physics*, Vol. 43, No. 2, 1981, pp. 357-372.

17. Van Leer, B., "Flux Vector Splitting for the Euler Equations," *Proceedings of the 8th International Conference on Numerical Methods in Fluid Dynamics*, Springer Verlag, Berlin, 1981.

18. Gupta, R. N., Lee, K. P., Zoby, E. V., Moss, J.N. And Thompson, R. A., "Hypersonic Viscous Shock-Layer Solutions over Long Slender Bodies - Part 1: High Reynolds Number Flows," *Journal of Spacecraft and Rockets*, Vol. 27, No. 2, pp. 175-184, March-April 1990.

19. Cooke, J. C., "An Axially Symmetric Analogue for General Three-Dimensional Boundary Layers," Reports and Memoranda 3200, 1961.

20. Zoby, E. V. and Simmonds, A. L., "Engineering Flow Field Method with Angle-of-Attack Applications," *Journal of Spacecraft and Rockets*, Vol. 22, No. 4, 1985, pp. 398-405.

21. Yee, H. C., "On Symmetric and Upwind TVD Schemes," NASA TM 88325, 1990.

22. Micol, J. R. "Hypersonic Aerodynamic/ Aerothermodynamic Testing Capabilities at Langley Research Center: Aerothermodynamic Facilities Complex," AIAA Paper 95-2107, June 1995.

23. Alter, S. J., "Grid Generation Techniques Utilizing the Volume Grid Manipulator," AIAA Paper 98-3012, June 1998.

24. Alter, S. J., "The Volume Grid Manipulator (VGM): A Grid Reusability Tool," NASA CR-4772, April 1997.

25. Harten, A., "High Resolution Schemes for Hyperbolic Conservation Laws," *Journal of Computational Physics*, Vol. 49, No. 3, 1983, pp. 357-393.

26. Roe, P. L., "Some Contributions to the Modelling of Discontinuous Flows," *Proceedings of the 1983 AMS-SIAM Summer Seminar on Large Scale Computing in Fluid Mechanics, Lectures in Applied Mathematics*, Vol. 22, pp.163-193, SIAN, Philadelphia, 1985.
27. Chakravarthy, S. R., and Osher, S., "High Resolution Applications of the Osher Upwind Scheme for the Euler Equations," AIAA Paper 83-1943, 1983.
28. Merski, N. R., "Global Aeroheating Wind-Tunnel Measurements Using Improved Two-Color Phosphor Thermography Method," *Journal of Spacecraft and Rockets*, Vol. 36, No. 2, March-April 1999, pp. 160-170
29. Berry, S. A., Horvath, T. J., DiFulvio, M., Glass, C. E., and Merski, N. R., "X–34 Aeroheating at Mach 6 and Mach 10," AIAA Paper 98-0881, Jan. 1998.
30. Fay, J. A. and Riddell, F. R., "Theory of Stagnation Point Heat Transfer in Dissociated Air," *Journal of Aeronautical Sciences*, Vol. 15, No. 2., 1958.
31. Cheatwood, F. A., and Thompson, R. A., "The Addition of Algebraic Turbulence Modeling to Program LAURA," NASA TM 107758, April 1993.

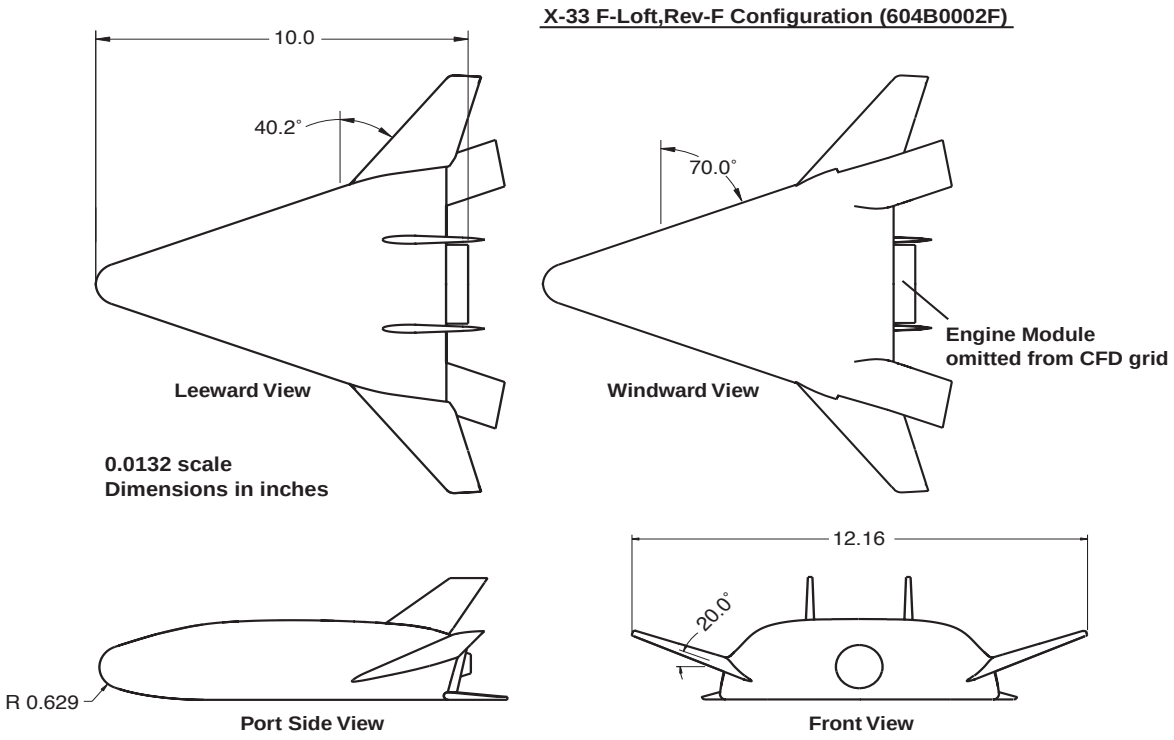

Figure 1. X-33 604B0002F (F-Loft, Rev-F) Configuration, 1.32% of Full Scale, Dimensions in Inches

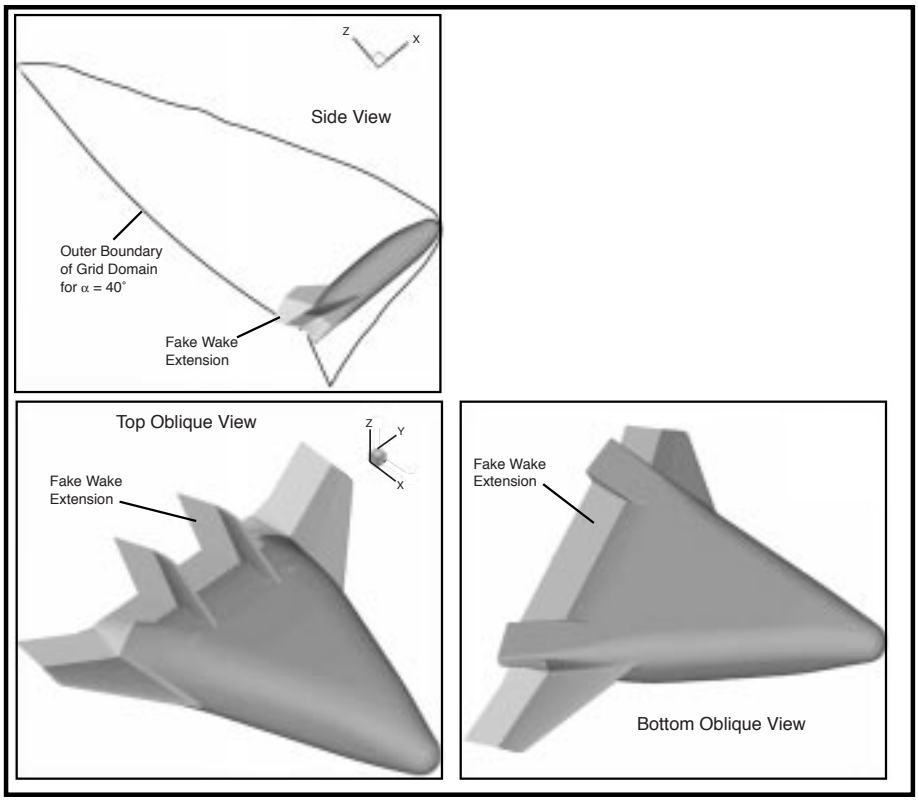

Figure 2. X-33 Computational Surface Geometry with Fake-Wake Extension

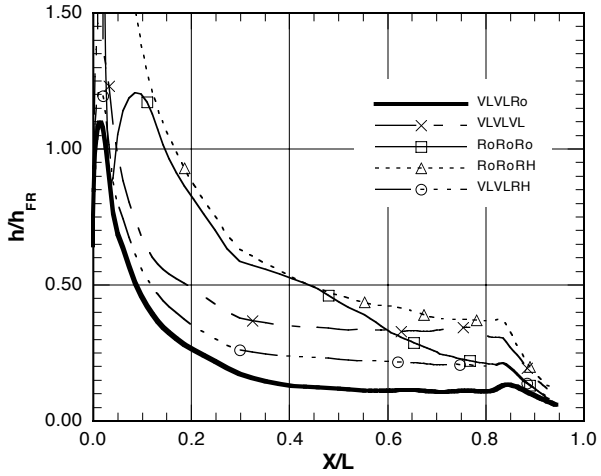

Figure 3. Effect of Flux Formulation on Centerline Heating Distribution, $\alpha = 40^{\circ}$

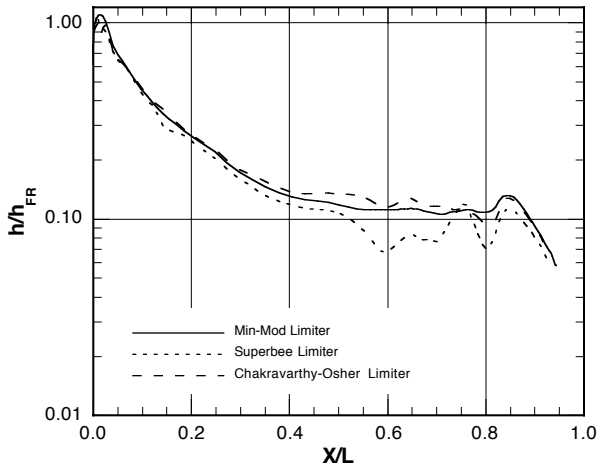

Figure 4. Effect of TVD Limiter on Centerline Heating Distribution, $\alpha = 40^{\circ}$

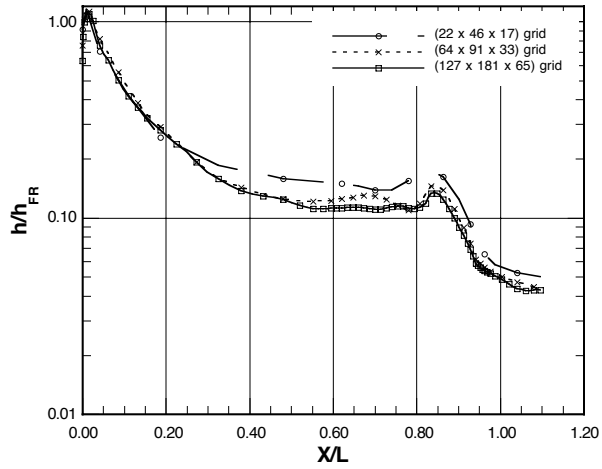

Figure 5. Grid Resolution Effects on Computed Centerline Heating Distribution, $\alpha = 30^{\circ}$

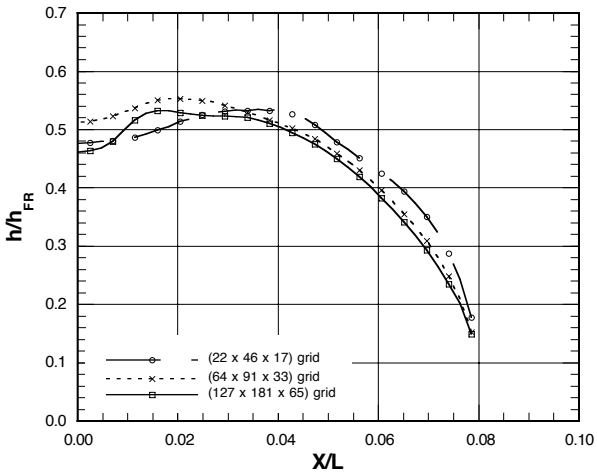

Figure 6. Grid Resolution Effects on Computed Axial Heating Distribution at X/L= 0.1, $\alpha = 30^{\circ}$

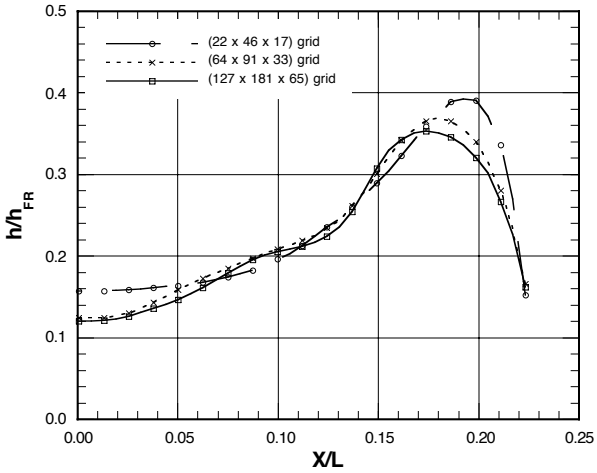

Figure 7. Grid Resolution Effects on Computed Axial Heating Distribution at X/L= 0.5, $\alpha = 30^{\circ}$

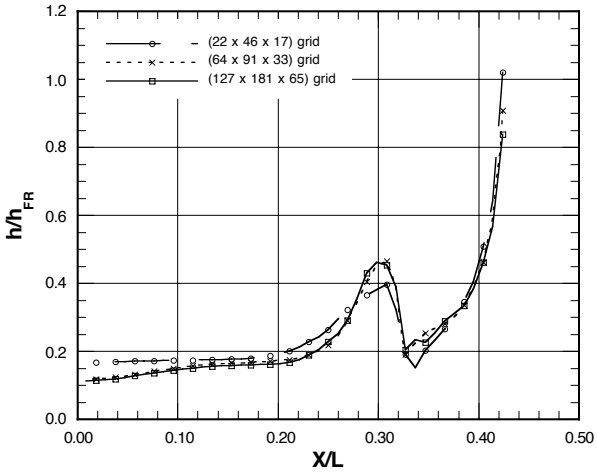

Figure 8. Grid Resolution Effects on Computed Axial Heating Distribution at X/L = 0.8, $\alpha = 30^{\circ}$

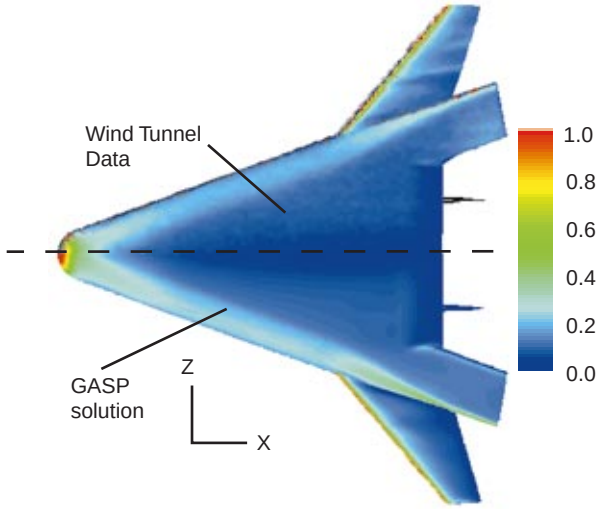

Figure 9. Global Comparison of GASP Computation and Tunnel Data, $\alpha = 20^\circ$, Windward View

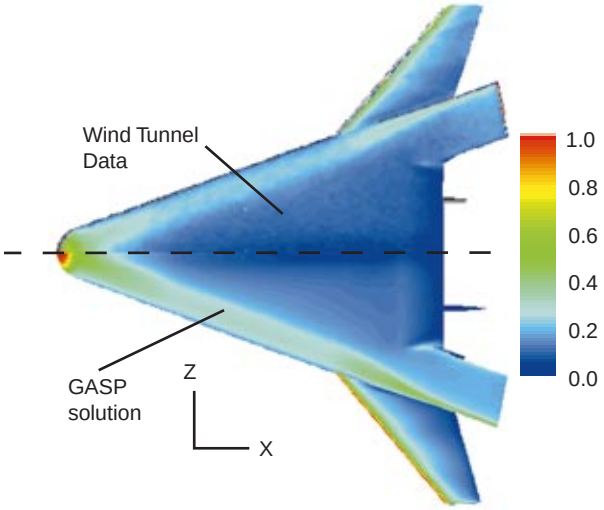

Figure 10. Global Comparison of GASP Computation and Tunnel Data, $\alpha = 30^\circ$, Windward View

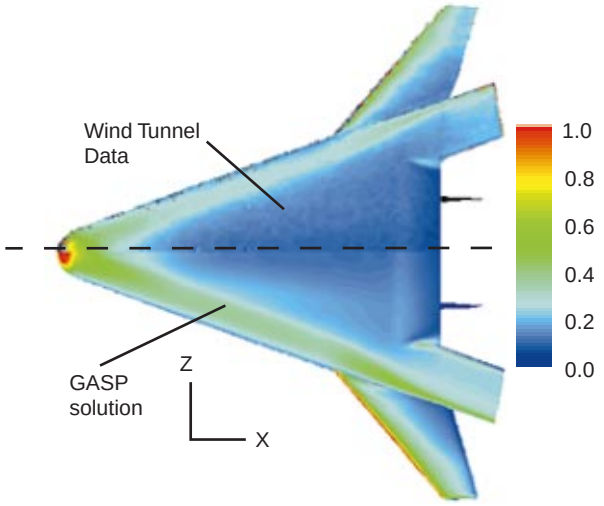

Figure 11. Global Comparison of GASP Computation and Tunnel Data, $\alpha = 40^\circ$, Windward View

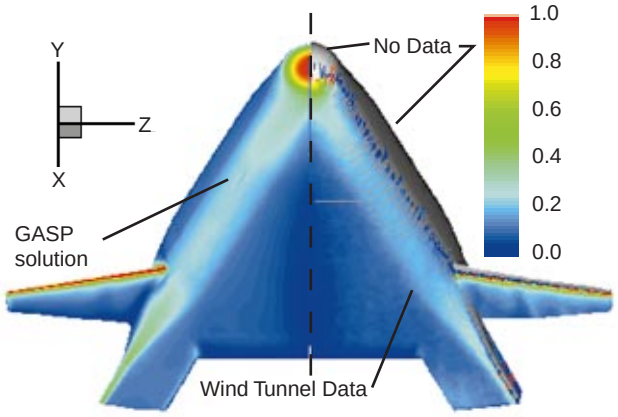

Figure 12. Global Comparison of GASP Solution and Tunnel Data, $\alpha = 20^\circ$, Front View

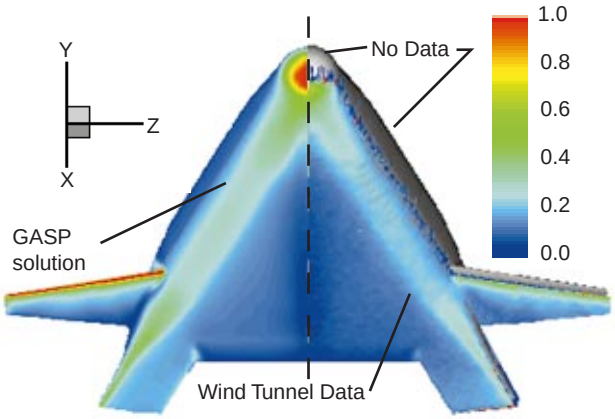

Figure 13. Global Comparison of GASP Solution and Tunnel Data, $\alpha = 30^\circ$, Front View

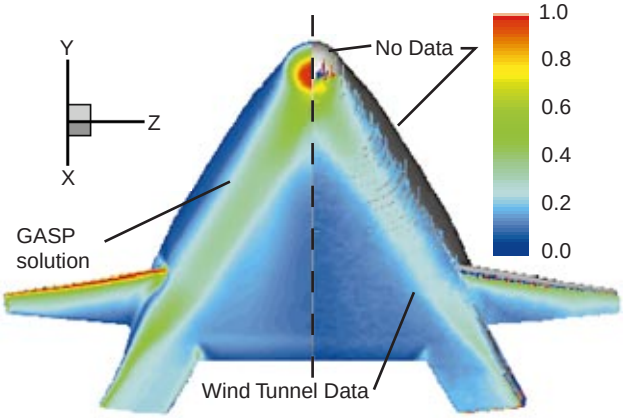

Figure 14. Global Comparison of GASP Solution and Tunnel Data, $\alpha = 20^\circ$, Front View

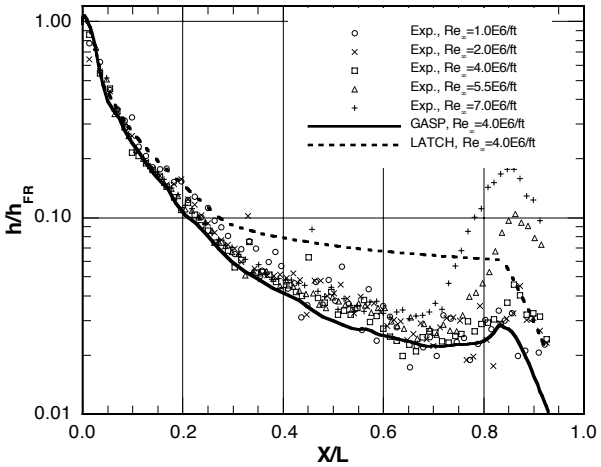

Figure 15. Windward Centerline Heating Data Comparison with Laminar Computations at α=20°

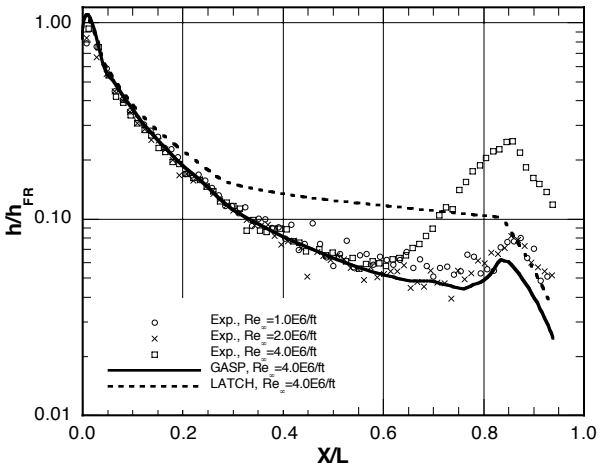

Figure 16. Windward Centerline Heating Data Comparison with Laminar Computations at α=30°

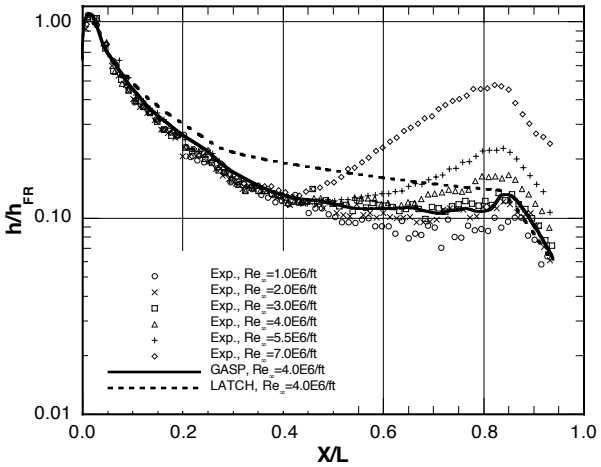

Figure 17. Windward Centerline Heating Data Comparison with Laminar Computations at α=40°

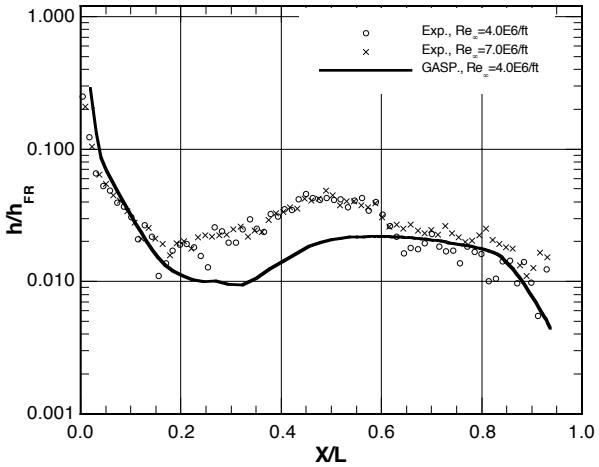

Figure 18. Leeward Centerline Heating Data Comparison with Laminar Computations at α=20°

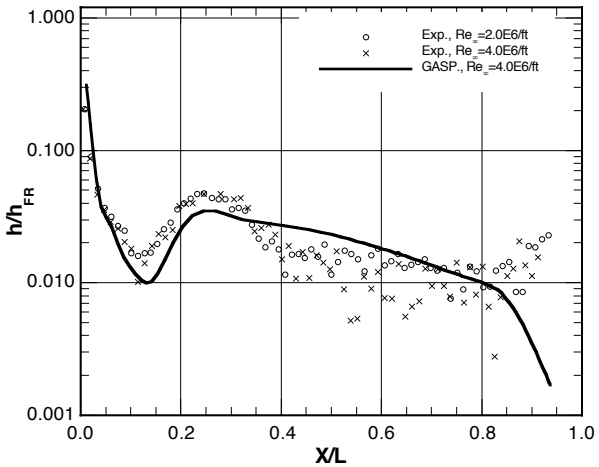

Figure 19. Leeward Centerline Heating Data Comparison with Laminar Computations at α=30°

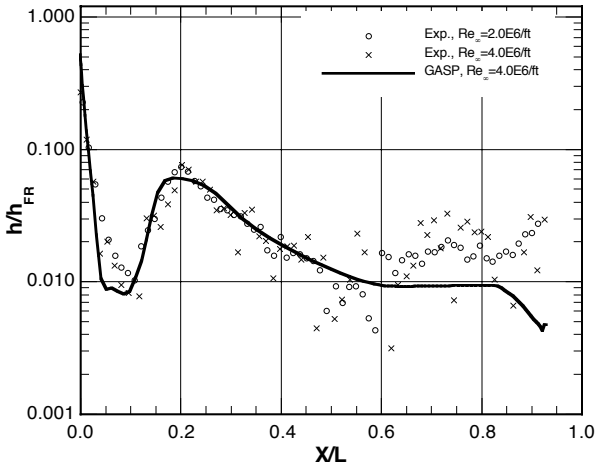

Figure 20. Leeward Centerline Heating Data Comparison with Laminar Computations at α=40°

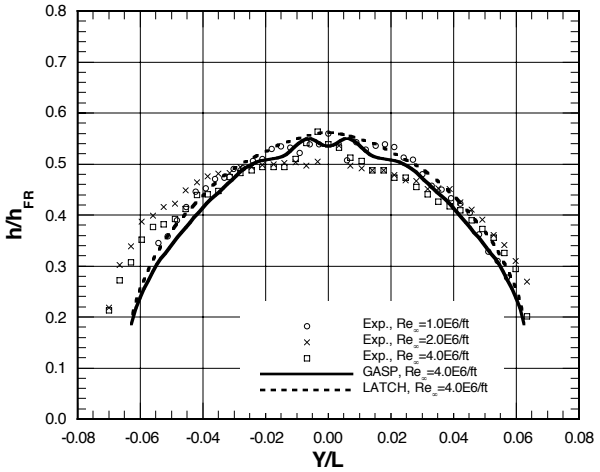

Figure 21. Axial Heating Data Comparison with Laminar Computations at X/L=0.05 for $\alpha = 30^{\circ}$

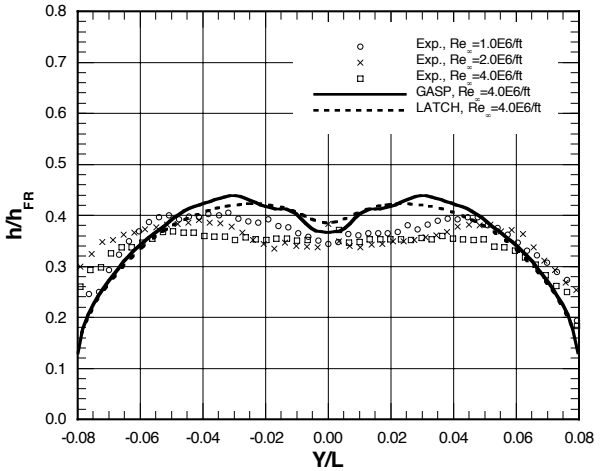

Figure 22. Axial Heating Data Comparison with Laminar Computations at X/L=0.10 for $\alpha = 30^{\circ}$

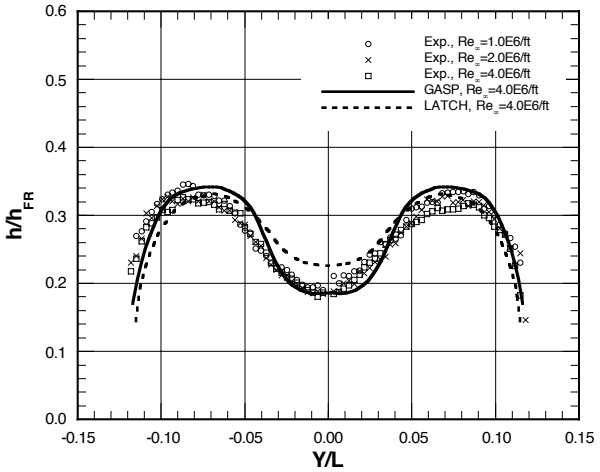

Figure 23. Axial Heating Data Comparison with Laminar Computations at X/L=0.20 for $\alpha = 30^{\circ}$

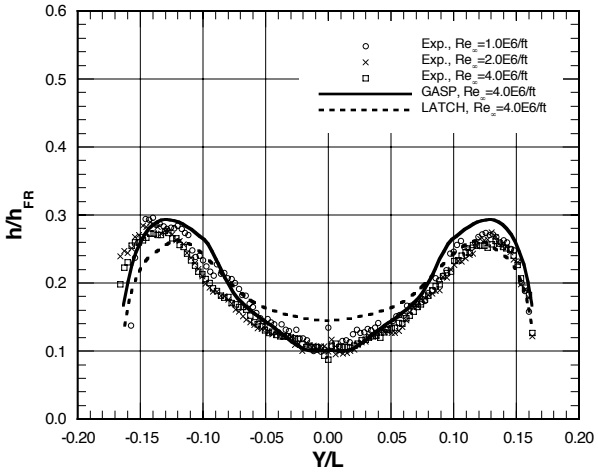

Figure 24. Axial Heating Data Comparison with Laminar Computations at X/L=0.32 for $\alpha = 30^{\circ}$

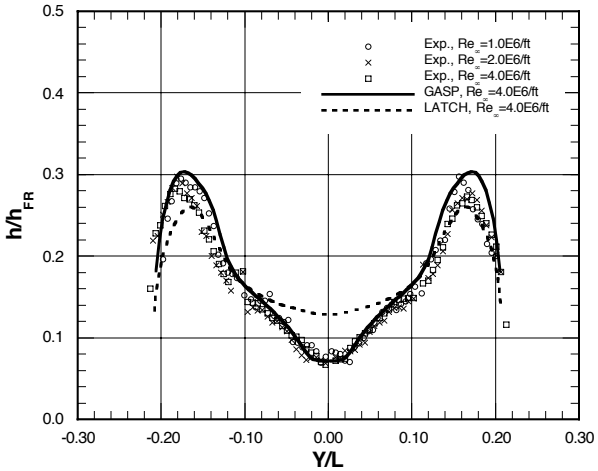

Figure 25. Axial Heating Data Comparison with Laminar Computations at X/L=0.45 for $\alpha = 30^{\circ}$

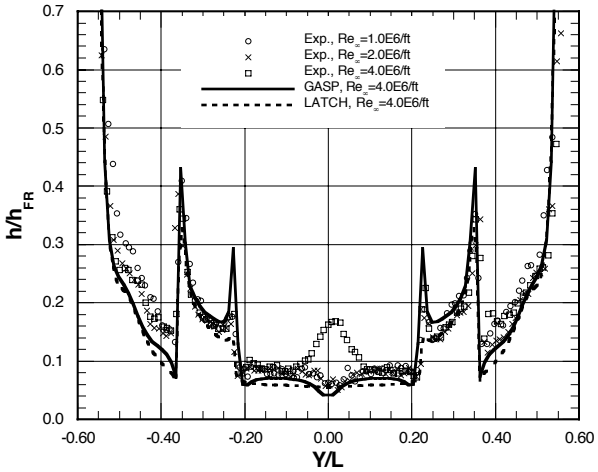

Figure 26. Axial Heating Data Comparison with Laminar Computations at X/L=0.90 for $\alpha = 30^{\circ}$

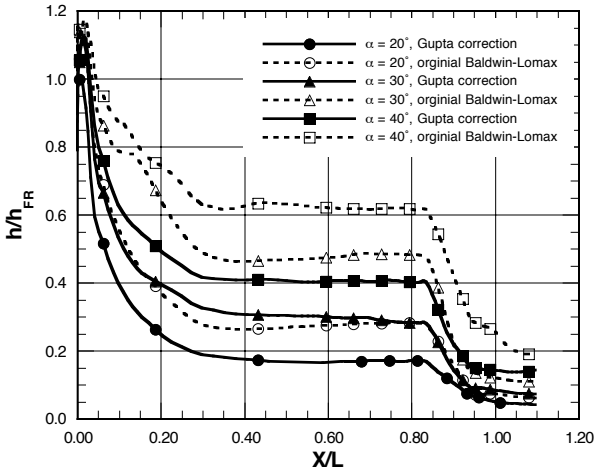

Figure 27. Comparison of Modified and Original Baldwin-Lomax Turbulent Heating Predictions (Mach 6 case)

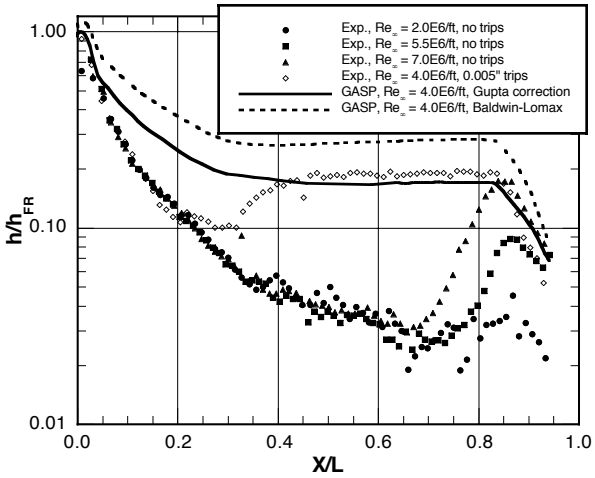

Figure 28. Windward Centerline Heating Data Comparison with Turbulent Computations at α=20°

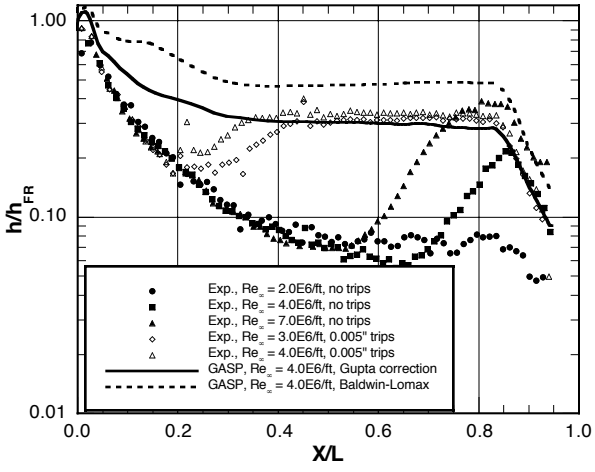

Figure 29. Windward Centerline Heating Data Comparison with Turbulent Computations at α=30°

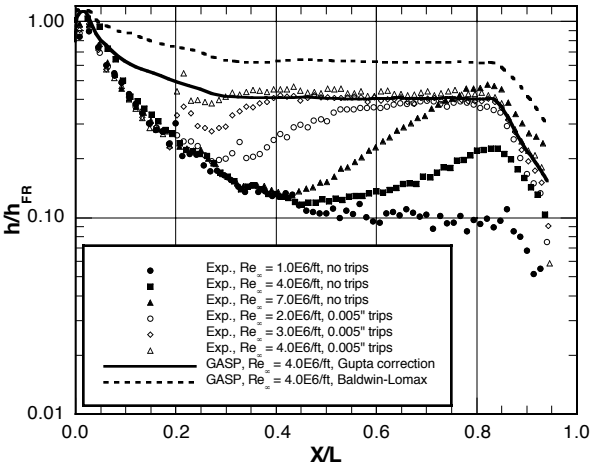

Figure 30. Windward Centerline Heating Data Comparison with Turbulent Computations at α=40°

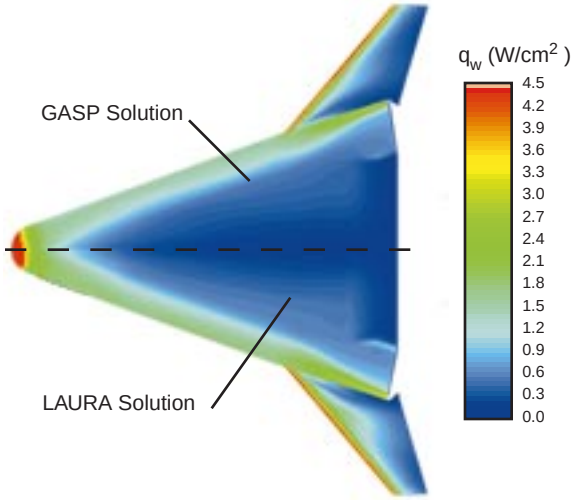

Figure 31. Windward Global Heating Comparison between GASP and LAURA for Flight Peak Heating Case

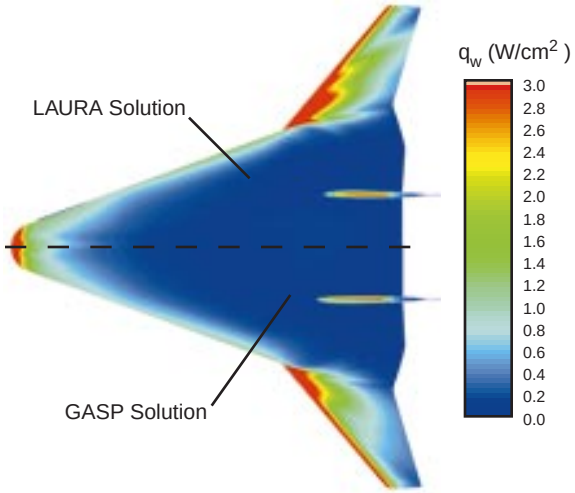

Figure 32. Leeward Global Heating Comparison between GASP and LAURA for Flight Peak Heating Case

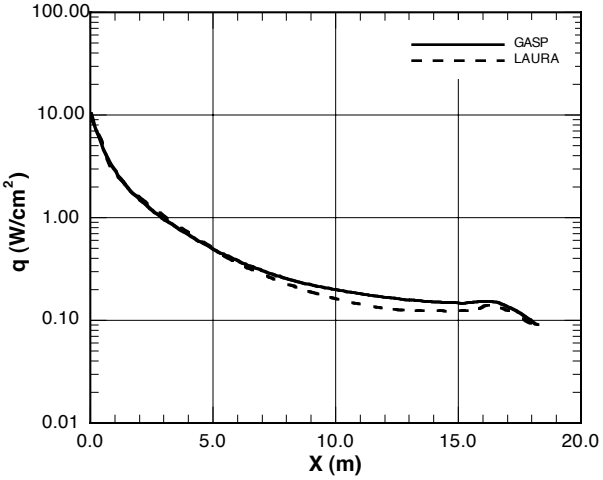

Figure 33. Windward Centerline Comparison for Flight Peak Heating Case (Mach 8.83, α = 10°)

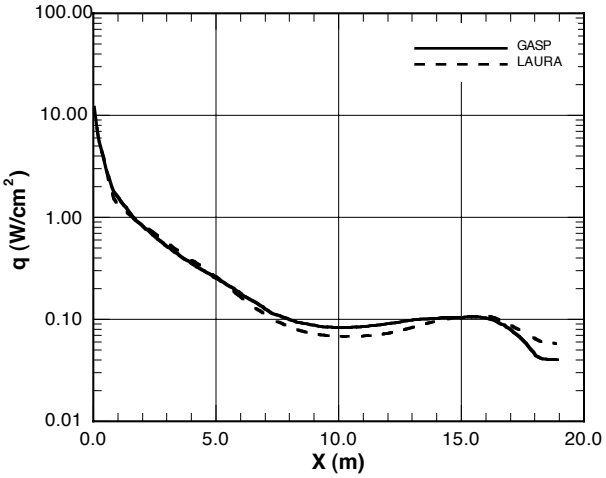

Figure 34. Leeward Centerline Comparison for Flight Peak Heating Case (Mach 8.83, α = 10°)

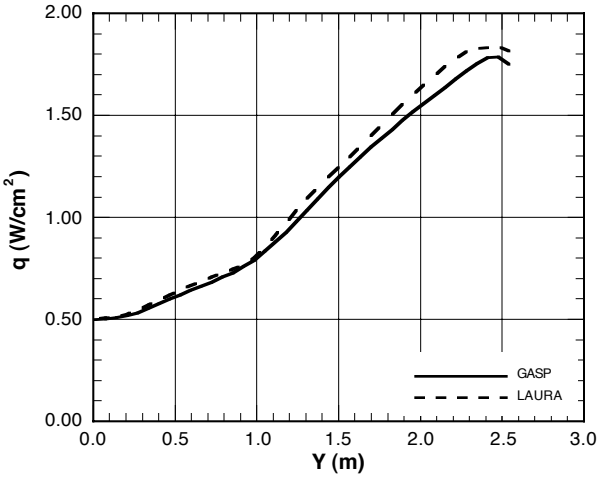

Figure 35. Windward Axial Comparison at X= 5.0 m for Flight Peak Heating Case (Mach 8.83, α = 10°)

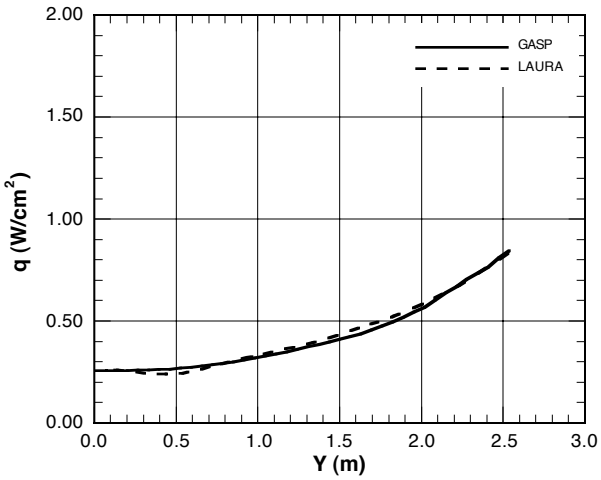

Figure 36. Leeward Axial Comparison at X= 5.0 m for Flight Peak Heating Case (Mach 8.83, α = 10°)

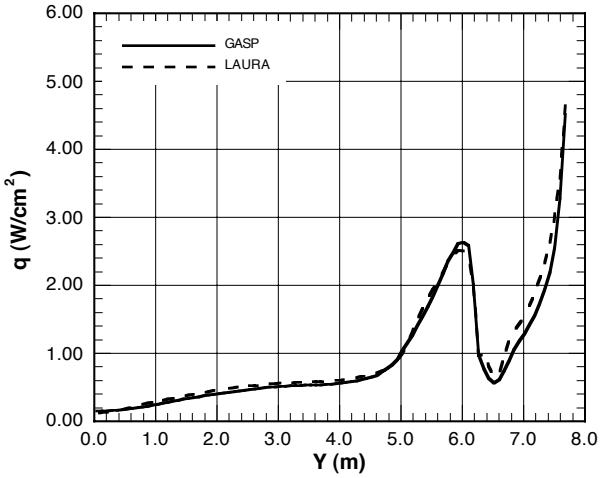

Figure 37. Windward Axial Comparison at X = 15.0 m for Flight Peak Heating Case (Mach 8.83, α = 10°)

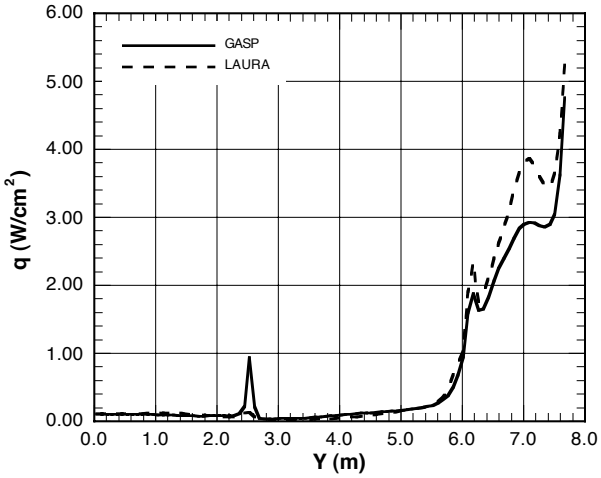

Figure 38. Leeward Axial Comparison at X = 15.0 m for Flight Peak Heating Case (Mach 8.83, α = 10°)